

RESEARCH ARTICLE

The evaluation of the diffuse interface method for phase change simulations using OpenFOAM

Nima Samkhaniani | Mohamad Reza Ansari

Faculty of Mechanical Engineering, Tarbiat
Modares University, Tehran, I.R. of Iran

Correspondence

Nima Samkhaniani, Faculty of Mechanical
Engineering, Tarbiat Modares University,
P.O. Box 14117 13116, Tehran, I.R. of Iran
Email: nima.samkhaniani@modares.ac.ir,
nima.samkhaniani@gmail.com

Abstract

In the present study, a new solver named phaseChangeHeatFoam is implemented on the OpenFOAM cfd package to simulate boiling and condensation. The solver is capturing the interface between two immiscible phases with a color function volume of fluid (CF-VOF) method. The two fluids (vapor and liquid) are assumed Newtonian and incompressible. The surface tension is modeled with continuous surface force (CSF) which is improved with a Lafaurie filter to suppress the spurious current. The mass flux across the interface in the phase change process is determined by either Lee or Tanasawa mass transfer models. Additionally, the slight variation of saturation temperature with local pressure is considered with the simplified Clausius–Clapeyron relation. The coupled velocity pressure equation is solved using the PIMPLE algorithm. The new solver is validated and examined with (i) Stefan problem, (ii) two-dimensional film boiling, (iii) the film condensation on a horizontal plate, (iv) the laminar film condensation over a vertical plate, and (v) bubble condensation in subcooled

Nomenclature: C_a , Compression factor (–); C_p , Specific heat (J/kgK); d_L , Liquid thermal diffusivity: $k/\rho C_p$ (m²/s); D , Equivalent diameter (M); D_0 , Bubble Initial diameter (M); \vec{g} , gravity acceleration (m/s²); H_{LG} , Latent heat (J/kg); k , Thermal conductivity (W/mK); M , Molar mass (kg/Kmol); \dot{m}'' , mass flow rate per unit area (kg/m²s); \dot{m}''' , mass flow rate per unit volume (kg/m³s); P , Pressure (Pa); P_{rgh} , Dynamic Pressure (Pa); r , Mass transfer intensity factor (1/s); R , Universal gas constant (J/mol K); T , Temperature (K); W , width (M); \vec{U} , velocity (m/s); \vec{U}_c , Compressive velocity (m/s)

Greek symbols: α , Volume fraction factor; κ , Interface curvature (m^{–1}); μ , Dynamic viscosity (Pa.s); λ , Taylor unstable wave (M); ρ , Density (kg/m³); γ , Tanasawa Coefficient (–); σ , Surface Tension (N/m)

Subscripts: c , Condensation; e , Evaporation; G , Gas (vapor) phase; L , Liquid phase; sat , Saturation; sub , Subcooled; sup , Superheat; W , wall

boiling. The present study shows the capability of a diffuse interface method in accurate simulation of the phase change process and it is expected to be instructive for further numerical studies in this area.

KEYWORDS

boiling, condensation, interFoam, OpenFOAM, volume of fluid

1 | INTRODUCTION

1.1 | Importance of predictive tools for phase change phenomena

The diabatic flows have significant industrial importance in heating and cooling systems. Two-phase flow heating and cooling systems have gained significant popularity in recent years due to an urgent need to overcome heat dissipation challenges in aerospace and commercial electronic devices. Heat dissipation rates at such devices are no longer manageable with single phase cooling system. Therefore, more aggressive two-phase solutions are being sought. Recent studies concerning the development of two-phase cooling solutions have focused on heat acquisition or rejection by boiling and condensation, respectively. While empirical formulations constitute the most popular means for predicting transport behavior in designing cooling system, these formulations are limited by working fluids, geometries, and operating conditions of databases upon which they are based. In order to achieve more universal predictive tools, there is a desire to develop computational techniques.

1.2 | Application of numerical models in phase change system

Several types of approaches such as Lagrangian, Eulerian, and Eulerian–Lagrangian have been developed for simulation of two-phase systems in recent decades.

The Lagrangian or Eulerian–Lagrangian approaches such as smoothed-Particle Hydrodynamic (SPH)¹ and front tracking (FT)² are limited to simple cases due to the complexity of applying complicated grid topologies. Hence, Eulerian methods are more popular due to their simplicity and feasibility of tackling multiple interfaces.

The two main representative examples of Eulerian approach are Level-Set (LS)³ and volume of fluid (VOF).⁴ There are also several Hybrid methods⁵ such as CLSVOF or VOSET which are couple of level set and volume of fluid approaches.^{6–10} The numerical method in this approach is classified based on the thickness of interface. An interface is the thin boundary layer that separates two distinct phases of matter. The interface thickness in the numerical method as shown in Fig. 1 is zero (sharp) or finite (diffusive). In sharp interface methods, the physical interface is a functional interface of zero thickness and physical quantities such as density and viscosity are discontinuous at the interface. Volume of fluid method with interface reconstruction such as PLIC¹¹ and PROST¹² are two examples of the sharp interface method. In diffuse interface methods such as CICSAM¹³ and THINC,¹⁴ the interface has a finite thickness and physical quantities vary continuously across the interface. However, the numerical interface thickness in the diffuse method is much larger than the actual physical thickness which is for a liquid–fluid interface typically a few nanometers.¹⁵ The main disadvantage of interface reconstruction volume of fluid (IR-VOF) is the complexity of the interface reconstruction, especially in 3D simulations

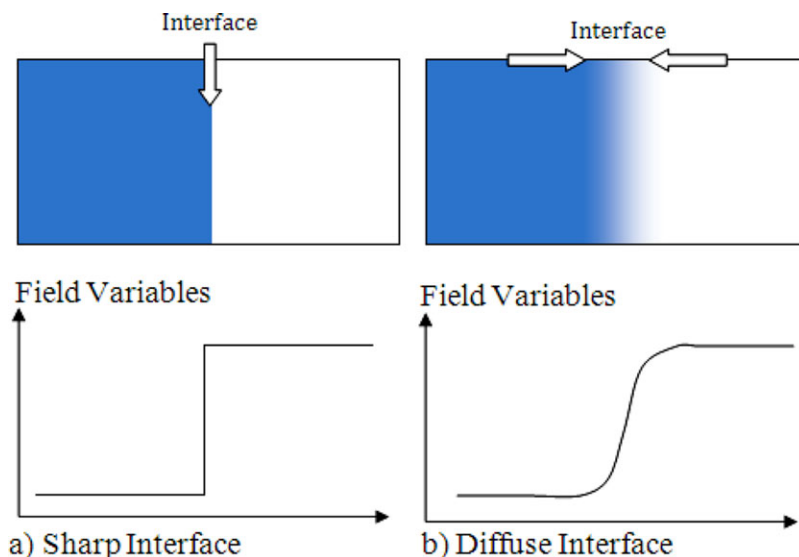


FIGURE 1 Comparison of sharp and diffuse interface methods

and physics involving extensive topology changes. Therefore, volume of fluid method without interface reconstruction which called color function volume of fluid has gained more popularity.

The Eulerian approach has been developed to simulate flow with phase change in the last decades. Welch and Wilson¹⁶ introduced a PLIC-VOF approach for simulation of boiling. Hardt and Wondra¹⁷ proposed an evaporation model that relies on a continuum field representation of the source terms in the mass conservation equation and applied on PLIC-VOF in Fluent software. In order to simulate evaporating droplets, Schlottke and Weigand¹⁸ developed a PLIC-VOF method which involves two VOF variables, one for the Liquid phase and one for the vapor phase. Son and Dhir¹⁹ and Son et al.²⁰ modified the Level set method to account for phase change. They assumed that the vapor phase is at saturation temperature, so they solved the energy equation only for the liquid phase. Level set methods for incompressible flow with phase change are also presented by Tanguy et al.²¹ and Gibou et al.²² who applied the ghost fluid approach to impose the jump conditions at the interface. A CLSVOF method for simulation of bubble growth in film boiling was developed by Tomar et al.²³ Guo et al.⁶⁴ simulated film boiling using VOSET method. Kunkelmann and Stephan²⁴ simulated nucleating boiling with special treatment for heat flux in contact angle.

There are several Eulerian codes to simulate multiphase flows, a color function volume of fluid (CF-VOF) solver named *interFoam* in open source CFD package OpenFOAM²⁵ has been receiving an increased amount of attention and usage.^{26–28} This VOF solver was implemented by Ubbink²⁹ at first, then it has undergone several modifications. The present code is a part of C++ libraries of OpenFOAM. This software was designed for finite volume discretization of a generic set of partial differential equations. However, several useful features such as ease of parallelization, availability of preprocessing and post processing utilities, error checks and choice of spatial and temporal discretization schemes make the code attractive for research. *InterFoam* has been recently contributed to consider phase change phenomena (boiling and condensation). Table 1 provides a comprehensive summary of literature concerning the implementation of different computational phase change model using OpenFOAM.

TABLE 1 Summary of computational phase change simulation in OpenFOAM frame work

Author	Applications	Model	Remarks
Kunkelmann and Stephan ³⁰	Nucleate boiling	Tanasawa	axisymmetric grid, 3-dimensional grid with adaptive grid refinement, contact line model for evaporation, VOF
Kunkelmann and Stephan ²⁴	Nucleate boiling	Sharp interface model	axisymmetric grid, couple of level set and VOF,
Zeng et al. ³¹	Bubble condensation	Tanasawa	3-dimensional grid, simple couple of level set and VOF
Doro ³²	Falling film evaporation	Tanasawa	2-dimensional grid, laminar, VOF
Rattner and Garimella ³³	Film condensation	–	2-dimensional grid, laminar, VOF, new phase change model
Bahreini et al. ³⁴	Bubble condensation	Lee	2-dimensional grid, laminar, VOF

1.3 | Phase change models

1.3.1 | Tanasawa model

Scharge³⁵ proposed a phase change model based on the Hertz–Knudsen equation,³⁶ with the interfacial jump in the temperature and pressure $T_{sat}(P_L) = T_L \neq T_{sat}(P_G) = T_G$. Mass flux at the interface is given by

$$\dot{m}'' = \frac{2}{2 - \gamma_c} \sqrt{\frac{M}{2\pi R}} \left[\gamma_c \frac{P_G}{\sqrt{T_G}} - \gamma_e \frac{P_L}{\sqrt{T_L}} \right], \quad (1)$$

where $R = 8.314 \text{ J/mol K}$ is the universal gas constant, γ the fraction of molecules transferred from one phase to the other during phase change. The subscripts c and e in the equation refer to condensation and evaporation, respectively. Here $\gamma_e = 1$ and γ_c represent complete evaporation and complete condensation, respectively. In phase change simulation, usually equal values of γ_c and γ_e are considered. While $\gamma = 0.1 - 1$ for dynamically renewing water surfaces such as jets and moving films and $\gamma < 0.1$ for stagnant surfaces are recommended.³⁷ Tanasawa³⁸ simplified Eq. (1) using extra assumptions. He assumed that the interface is at saturation temperature and the heat flux linearly dependent on the temperature jump between the interface and the vapor. The mass flux rate in Tanasawa's model is given by

$$\dot{m}'' = \frac{2\gamma}{2 - \gamma} \sqrt{\frac{M}{2\pi R}} \frac{\rho_G H_{LG}(T - T_{sat})}{T_{sat}^{3/2}}, \quad (2)$$

where T_{sat} is based on local pressure. The volumetric transferred mass rate in ($\text{kg/m}^3\text{s}$) is defined as

$$\dot{m}''' = \dot{m}'' |\nabla \alpha_L|. \quad (3)$$

1.3.2 | Lee model

Lee³⁹ assumed that mass is transferred at a constant pressure in phase change flow and derived a model for a quasi-thermo-equilibrium state. The volumetric transferred mass rate is given by

$$\dot{m}''' = r_c(1 - \alpha_L)\rho_G \frac{T - T_{sat}}{T_{sat}}, \quad \text{for condensation } T < T_{sat} \quad (4)$$

and

$$\dot{m}''' = r_e \alpha_L \rho_L \frac{T - T_{sat}}{T_{sat}}, \quad \text{for evaporation } T > T_{sat}, \quad (5)$$

where r_c and r_e in s^{-1} are empirical coefficients called the mass transfer intensity factor. The extensive ranges from 0.1 to 10^7 have been conducted in literature for r .^{40–45}

1.3.3 | Sharp interface model

The sharp interface model is based on the Rankine–Hugoniot jump condition for energy conservation where all the heat transferred at the interface is assumed to be consumed by latent heat due to phase change and given by

$$\dot{m}''' = \frac{k_{eff}(\nabla \alpha_L \cdot \nabla T)}{H_{LG}}, \quad (6)$$

where k_{eff} is the effective thermal conductivity, which can be determined from the volume fractions and thermal conductivities of the vapor and liquid.⁴⁶

1.4 | Objectives of study

The sharp interface method is the preference in the implementation of the phase change process, the capability of the diffuse interface method in correct simulation of phase change phenomena is not well defined. In addition, despite several implementations of the phase change model (boiling or condensation) in the framework of OpenFOAM, there is no exclusive and detailed documented resource, and proposed numerical methods are often validated for user specific interest. Therefore, in the present study a solver called “phaseChangeHeatFoam” is developed to simulate boiling and condensation. This article provides detailed information on governing equation, code structure, and numerical method for implementing the phase change process in the framework of OpenFOAM. Moreover, this study provides several problems to investigate the performance of the present implementation.

2. | COMPUTATIONAL METHOD

2.1 | Governing equations

In this study, both vapor liquid phases are assumed incompressible and immiscible. The volume of fluid method uses a discontinuous scalar color function to resolve the interface among two phases in

fixed grids. This scalar function is the ratio of one fluid volume to the volume of cell, and it is defined as

$$\alpha_L(\vec{x}, t) = \frac{V_{Liquid}}{V} = \begin{cases} 1 & \vec{x} \in \text{Liquid} \\ 0 < \alpha_L < 1 & \vec{x} \in \text{interface} \\ 0 & \vec{x} \in \text{vapor} \end{cases} \quad (7)$$

The thermo-physical properties of two-phase flow such as viscosity (μ), density (ρ), and thermal conductivity (k) are defined as

$$y = \alpha_L y_L + (1.0 - \alpha_L) y_G, \quad y \in [\mu, \rho, k], \quad (8)$$

where y has liquid physical properties where $\alpha_L = 1.0$, and it has vapor physical properties where $\alpha_L = 0.0$. The interface is moving along the flow; therefore the volume fraction is advected to keep the interface. In order to derive the transport equation for volume fraction, density (ρ) from Eq. (8) is placed in Eq. (9) and rearranged to obtain Eq. (10). Eq. (9) indicates the global continuity equation

$$\frac{\partial}{\partial t}(\rho) + \nabla \cdot (\rho \vec{U}) = 0, \quad (9)$$

$$\frac{\partial \alpha_L}{\partial t} + \vec{U} \cdot \nabla \alpha_L + \alpha_L \nabla \cdot \vec{U} = - \frac{\rho_G \nabla \cdot \vec{U}}{(\rho_L - \rho_G)}, \quad (10)$$

where $\nabla \cdot \vec{U}$ is zero in an incompressible adiabatic two-phase flow. In the phase change process, it is determined from the local continuity for each phase:

$$\frac{\partial}{\partial t}(\rho_L) + \nabla \cdot (\rho_L \vec{U}) = -\dot{m}''', \quad (11)$$

$$\frac{\partial}{\partial t}(\rho_G) + \nabla \cdot (\rho_G \vec{U}) = +\dot{m}'''. \quad (12)$$

As both phases are incompressible, the first term on the left hand of Eqs. (11) and (12) is zero. Then, by using the integral approach and divergence theorem, Eqs. (11) and (12) are converted to the following equations:

$$\int_L \vec{U} \cdot \vec{n}_L dS_L = -\frac{\dot{m}}{\rho_L}, \quad (13)$$

$$\int_G \vec{U} \cdot \vec{n}_G dS_G = +\frac{\dot{m}}{\rho_G}. \quad (14)$$

The unit normal vector at the interface is displayed in Fig. 2. As $\vec{n}_G = \vec{n}_I = -\vec{n}_L$, then the summation of the former equations results in

$$\int_S \vec{U} \cdot \vec{n} dS = \dot{m} \left(\frac{1}{\rho_G} - \frac{1}{\rho_L} \right). \quad (15)$$

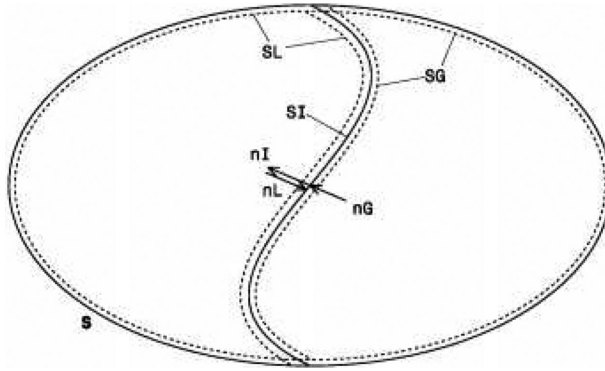


FIGURE 2 Two-phase flow system, S denotes surface and n denotes unit normal, L: liquid, G: vapor, and I: interface

The differential form of Eq. (15) is

$$\nabla \cdot \vec{U} = \dot{m}''' \left(\frac{1}{\rho_G} - \frac{1}{\rho_L} \right). \quad (16)$$

By replacing Eq. (16) into Eq. (10), the following transport equation for α_L is derived:

$$\frac{\partial \alpha_L}{\partial t} + \vec{U} \cdot \nabla \alpha_L = -\dot{m}''' \left[\frac{1}{\rho_L} - \alpha_L \left(\frac{1}{\rho_L} - \frac{1}{\rho_G} \right) \right]. \quad (17)$$

In OpenFOAM, the extra divergence term is added to Eq. (17). This term contributes only in the region of the interface ($0 < \alpha_L < 1.0$). It limits the smearing of the interface because of the compensation of the diffusive fluxes²⁸

$$\frac{\partial \alpha_L}{\partial t} + \vec{U} \cdot \nabla \alpha_L + \nabla \cdot (\alpha_L (1 - \alpha_L) \vec{U}_c) = -\dot{m}''' \left[\frac{1}{\rho_L} - \alpha_L \left(\frac{1}{\rho_L} - \frac{1}{\rho_G} \right) \right]. \quad (18)$$

Here \vec{U}_c is compressive velocity. It is calculated in the normal direction to the interface to avoid any dispersion.⁴⁷ It is defined as

$$\vec{U}_c = \min\{C_\alpha |U|, \max(|U|)\} \frac{\nabla \alpha_L}{|\nabla \alpha_L|}. \quad (19)$$

The coefficient C_α controls the weight of the compression flux and should usually be in the range of unity ($1.0 < C_\alpha < 4.0$).^{28,48,49} In the present study, the compression factor $C_\alpha = 1.0$ is applied. The large compression factor increases the non-physical spurious current in the vicinity of the interface.

The momentum equation is given by

$$\frac{\partial(\rho \vec{U})}{\partial t} + \nabla \cdot (\rho \vec{U} \vec{U}) - \nabla \cdot (\mu (\nabla \vec{U}^T + \nabla \vec{U})) = -\nabla P + \rho \vec{g} + \sigma \kappa \nabla \alpha_L. \quad (20)$$

The last term in the right hand of Eq. (20) is considering surface tension using the continuous surface force (CSF) model.⁵⁰ Where σ is the surface tension, and κ is the interface curvature and is defined as

$$\kappa = -\nabla \cdot \left(\frac{\nabla \alpha_L}{|\nabla \alpha_L|} \right), \quad (21)$$

where $\widetilde{\alpha}_L$ is a smoothed VOF function calculated from α_L by smoothing it over a finite region around the interface. In the VOF method, the fluid interface sharply changes over a thin region. This abrupt change of the VOF function creates errors in calculating the normal vectors and the curvature of the interface, which are used to evaluate the interfacial forces. These errors induce spurious currents in the interfacial region.^{28,51} The spurious currents create extra heat convection around the interface which increases local mass transfer. An easy way to suppress these artifacts is to compute the interface curvature from a smoothed VOF function. In the present study, the smoother proposed by Lafaurie et al.⁵² is applied:

$$\widetilde{\alpha}_{Lp} = \frac{\sum_{f=1}^n \alpha_{Lf} S_f}{\sum_{f=1}^n S_f}, \quad (22)$$

where S_f is the magnitude of face area, the subscript p denotes the cell index, and f denotes the face index. The interpolated value (α_{Lf}) at the face center is calculated using linear interpolation. The application of this filter can be repeated m times to get a smoothed field. It should be noted that smoothing tends to wipe out high curvature regions and should be applied only up to the level that is strictly necessary to sufficiently suppress parasitic currents. Hoang et al.⁵³ found that the magnitude of parasitic current decreases up to one order from $m = 0$ to $m = 2$ and only a slight further decrease was observed for $m > 2$. Therefore, in present study $m = 2$ is employed in all simulations.

Energy equation is given by

$$\frac{\partial}{\partial t}(\rho C_p T) + \nabla \cdot (\rho C_p U T) - \nabla \cdot (k \nabla T) = -\dot{m}''' H_{LG}, \quad (23)$$

where H_{LG} is latent heat coefficient. The last term in Eq. (23) is added to consider latent heat during phase change.

The interface temperature is often at saturation, it is almost constant during phase change. However, the slight variation in the quantity of saturation temperature as a function of local pressure is determined using a simplified version of the Clausius–Clapeyron relation which is based on ideal gas assumption for the vapor phase

$$\ln \frac{P_{sat,1}}{P_{sat,0}} = -\frac{M H_{LG}}{R} \left(\frac{1}{T_{sat,1}} - \frac{1}{T_{sat,0}} \right). \quad (24)$$

It is well known that numerical interfacial flow computations become more challenging when the imbalance of material properties between the phases increases.⁵¹ In order to reduce the material properties imbalance across the interface, and increase numerical robustness, Eq. (23) is rearranged as

$$\frac{\partial}{\partial t}(T) + \nabla \cdot (U T) - \nabla \cdot (D_k \nabla T) = -D_c \dot{m}''' H_{LG}, \quad (25)$$

where D_k and D_c are defined as

$$D_c = \frac{1.0}{\rho_L C_L \alpha_L + \rho_G C_G (1.0 - \alpha_L)}, \quad (26)$$

$$D_k = \frac{k_L \alpha_L + k_G (1.0 - \alpha_L)}{\rho_L C_L \alpha_L + \rho_G C_G (1.0 - \alpha_L)}. \quad (27)$$

To close the above set of equations, an appropriate phase change model is necessary to calculate transferred mass flux rate (\dot{m}'''). In the present study, Lee and Tanasawa mass transfer model are employed.

2.2 | Numerical details

In the present study, OpenFOAM which is an open source software is employed. It is a flexible and efficient C++ library for the customization and extension of applications (solvers and utilities) and operating on scalar, vectorial, and tensorial fields.²⁵ It is based on an unstructured mesh formulation with a collocated cell-centered variable arrangement and provides numerical methods for discretization of partial differential equations along with solvers for the corresponding numerical solution of the resulting system of algebraic equations. There are two main tensor derivative namespaces: the *fvm* (*finiteVolumeMethod*) namespace and the *fvc* (*finiteVolumeCalculus*) namespace to consider differential operators such as ∇ ., ∇^2 , $\frac{\partial}{\partial t}$. These differential operators correspond to *fvm::div()*, *fvm::laplacian()* and *fvm::ddt()* or alternatively *fvc::div()*, *fvc::laplacian()* and *fvc::ddt()* in OpenFOAM. The *fvc* functions perform an explicit evaluation of predetermined data and they map from one field to another. In contrast, *fvm* functions construct appropriate matrices using the finite volume discretization. They enable to create entire matrix representations of differential equations using *fvScalarMatrix* or *fvVectorMatrix* and their implicit numerical solution. These equation objects hold the matrices that represent the equations and handle the numerical solution. Moreover, there are geometric tensor field classes for example: *volScalarField* and *volVectorField* that contain field data on cell centers to represent field's variables such as velocity and pressure. The tensor field classes also have a reference to the mesh and include boundary information, previous time steps data which are necessary for temporal discretization, and SI dimension set information. Additionally, *surfaceScalarField* and *surfaceVectorField* are available which hold data at the center of surfaces of control volumes.

The present solver *phaseChangeHeatFoam* is developed on *interFoam* solver with OpenFOAM220. *InterFoam* is a solver for two incompressible, isothermal immiscible fluids using a volume of fluid phase-fraction based interface capturing approach. The momentum and other fluid properties are of the mixture and a single momentum equation is solved. In order to simulate boiling and condensation, the thermal energy transport equation (*TEqn.H*) is added to *interFoam*. Additionally, the volume fraction transport equation (*alphaEqn.H*) and momentum equations (*pEqn.H*) are modified with appropriate source terms. It provides support for generic phase-change models. Thus, phase-change models can be selected by the user during runtime, and new models can be rapidly incorporated. A summary of the *phaseChangeHeatFoam* algorithm is presented in Fig. 3.

In the beginning of the simulation, the solver loads the mesh and reads tensor fields (α_L , T , \vec{U} and P_{rgh}) and boundary conditions. $P_{rgh} = P - \rho gh$ is dynamic pressure and h is the fluid height. P_{rgh} is applied to avoid any sudden changes in the pressure at the boundaries for hydrostatic terms.

The main solver loop is then initiated. First, the time step is dynamically modified to ensure numerical stability. The adaptive time step is adjusted to satisfy the CFL condition and user-defined time step (*maxDeltaT*).²⁷ User-defined time step is employed to apply manually other temporal scales in the problem for instance the thermal diffusion time scale.³³

Next the discretized volume fraction Eq. (18) is solved for a user defined number of sub-time steps. Four sub-cycles are considered here. The volume fraction equation (*alphaEqn.H*) is modified as shown in Fig. 4. The volume fraction advection equation is solved using the multidimensional universal limiter with explicit solution (MULES) method which is based on the method of flux corrected transport (FCT) where an additional limiter is used to cutoff the face-fluxes at the critical values.⁵⁴ This solver is included in the OpenFOAM library, and performs the conservative transport equation of hyperbolic transport equations with defined bounds (0 and 1 for α_L).

Once the update phase field is obtained, the program updates thermo physical properties according to Eqs. (8), (26) and (27). Then the program enters the pressure-velocity loop. The process of correcting the pressure and velocity fields in sequence is known as pressure implicit with splitting of operators

Initialize simulation data, define vector and scalar field

While $t < \dots$ **DO**

1. Calculate Δ to insure CFL condition
2. Volume fraction sub-cycle, and update thermo physical properties
3. **PIMPLE** loop

- 3.1. Calculate momentum equation and form \vec{U}

- 3.2. **PISO** loop

- 3.2.1. Obtain and correct face flux (ϕ)

- 3.2.2. Solve P_{rgh} equation

- 3.3.3 Correct \vec{U}

4. Calculate T equation

Done

FIGURE 3 PhaseChangeHeatFoam algorithm summary

```

...
Pair<tmp<volScalarField> > vDotAlphal =
    twoPhaseProperties->vDotAlphal();
const volScalarField& vDotcAlphal = vDotAlphal[0]();
const volScalarField& vDotvAlphal = vDotAlphal[1]();

volScalarField Sp
(
    IOobject
    (
        "Sp",
        runTime.timeName(),
        mesh
    ),
    vDotvAlphal - vDotcAlphal
);

volScalarField Su
(
    IOobject
    (
        "Su",
        runTime.timeName(),
        mesh
    ),
    divU*alphal
    + vDotcAlphal
);

MULES::explicitSolve
(
    geometricOneField(),
    alphal,
    phi,
    phiAlpha,
    Sp,
    Su,
    1,
    0
);

```

FIGURE 4 Modified alphaEqn.H in phaseChangeHeatFoam

```

...
Pair<tmp<volScalarField> > vDotP = twoPhaseProperties->vDotP();
const volScalarField& vDotcP = vDotP[0]();
const volScalarField& vDotvP = vDotP[1]();

while (pimple.correctNonOrthogonal())
{
    fvScalarMatrix p_rghEqn
    (
        fvc::div(phiHbyA) - fvm::laplacian(rAUf, p_rgh)
        == fvm::Sp(vDotcP-vDotvP,p_rgh) - (vDotcP-vDotvP)*(pSat-rho*gh)
    );
}
...

```

FIGURE 5 Modified *pEqn.H* in *phaseChangeHeatFoam*

```

Pair<tmp<volScalarField> > vDotT = twoPhaseProperties->vDotT();
const volScalarField& vDotcT = vDotT[0]();
const volScalarField& vDotvT = vDotT[1]();

fvScalarMatrix TEqn
(
    fvm::ddt(T)
    + fvm::div(phi, T)
    - fvm::Sp(fvc::div(phi),T)
    - fvm::laplacian(k/rhoC, T,"laplacian(alphaEff,T)")
    == fvm::Sp(vDotcT-vDotvT,T) - (vDotcT-vDotvT)*TSatLocal
);

```

FIGURE 6 *TEqn.H* in *phaseChangeHeatFoam*

(PISO).⁵⁵ In the OpenFOAM frame work, PISO can be repeated for multiple iterations at each time step. This process is referred to as the PIMPLE loop. Here, only one outer correction is applied and the PIMPLE loop works in PISO mode. First, the matrix equation for the momentum equation is formed. Then the inner pressure–velocity correction process is initiated. In PISO, an intermediate velocity field is first obtained, and the cell-face volume fluxes (ϕ) are evaluated and corrected for gravitational forces, the continuum surface-tension force, and boundary conditions. The pressure–Poisson equation is then formed and solved. Following the approach of Ref. 25 the coefficients of the pressure equation are obtained from the diagonal entries of the momentum matrix equation (A_D). For condensing and evaporating flow, the pressure equation would be

$$\nabla \cdot \left(\frac{1}{A_D} \nabla p \right) = \nabla \cdot \phi - \dot{m}''' \left(\frac{1}{\rho_G} - \frac{1}{\rho_L} \right). \quad (28)$$

The last term on the left hand of Eq. (28) is considering the phase change process. The modified pressure equation (*pEqn.H*) is shown in Fig. 5. In order to avoid a checker-boarding effect in the momentum equation, the Rhie–Chow momentum interpolation⁵⁶ is applied.

Finally, the thermal energy transport equation (Eq. (25)) is solved. The *TEqn.H* is shown in Fig. 6. For numerical stability, source terms in *TEqn.H* and *pEqn.H* are linearized.

The terms *vDotAlpha*, *vDotP* and *vDotT* are mass flux rates which are calculated based on selected mass transfer models. Lee mass transform model implemented in *Lee.C* is shown in Fig. 7.

The discretization scheme is selectable by the user; in this series of simulations the schemes displayed in Table 2 are chosen. For convenience, the corresponding terminology of OpenFOAM is given.

```

Foam::Pair<Foam::tmp<Foam::volScalarField> >
Foam::phaseChangeTwoPhaseMixtures::Lee::mDotAlpha() const
{
    const volScalarField& T = alpha_.db().lookupObject<volScalarField>("T");

    return Pair<tmp<volScalarField> >
    (
        -rc_*rho2_*min(T-TSatLocal(),T0_)/TSatLocal()
        ,
        -rv_*rho1_*max(T-TSatLocal(),T0_)/TSatLocal()
    );
}

Foam::Pair<Foam::tmp<Foam::volScalarField> >
Foam::phaseChangeTwoPhaseMixtures::Lee::mDotP() const
{
    const volScalarField& T = alpha_.db().lookupObject<volScalarField>("T");
    const volScalarField& p = alpha_.db().lookupObject<volScalarField>("p");
    volScalarField limitedAlpha(min(max(alpha_, scalar(0)), scalar(1)));

    return Pair<tmp<volScalarField> >
    (
        -rc_*rho2_*min(T-TSatLocal(),T0_)/TSatLocal()
        *pos(p-pSat_)/max(p-pSat_,1E-06*pSat_)
        *(1.0 - limitedAlpha)
        ,
        -rv_*rho1_*max(T-TSatLocal(),T0_)/TSatLocal()
        *neg(p-pSat_)/max(pSat_-p,1E-06*pSat_)
        *limitedAlpha
    );
}

Foam::Pair<Foam::tmp<Foam::volScalarField> >
Foam::phaseChangeTwoPhaseMixtures::Lee::mDotT() const
{
    const volScalarField& T = alpha_.db().lookupObject<volScalarField>("T");
    volScalarField limitedAlpha(min(max(alpha_, scalar(0)), scalar(1)));

    return Pair<tmp<volScalarField> >
    (
        -rc_*rho2_*neg(T-TSatLocal())/TSatLocal()
        *(1.0 - limitedAlpha)
        ,
        rv_*rho1_*pos(T - TSatLocal())/TSatLocal()
        *limitedAlpha
    );
}

```

FIGURE 7 Lee.C in phaseChangeHeatFoam

3. | VALIDATION AND VERIFICATION

In this section, for validation of the present solver, five problems are considered. Among them, the Stefan problem, horizontal film condensation on a horizontal plate, and laminar film condensation on a vertical plate have analytical solutions. For the others including 2D film boiling and bubble condensations, the CFD result is compared with experimental data and correlations or previous numerical simulations using the sharp interface method. Since there is no interface reconstruction in the present VOF method, an iso-contour $\alpha_L = 0.5$ is assumed as the interface in all following simulations.

3.1 | Stefan problem

The one-dimensional Stefan problem is a well-known benchmark for boiling flow.^{16,17,60,61} A vapor film separates saturated liquid from a super-heated wall. Liquid and vapor are initially in quiescent

TABLE 2 Discretization and interpolation schemes of the numerical model

Term	Discretization scheme	Method
$\frac{\partial}{\partial t}(\rho \vec{U}), \frac{\partial}{\partial t}(\rho \vec{U}T)$	<i>Euler</i>	The first-order bounded implicit scheme
$\nabla \cdot (\rho \vec{U} \vec{U})$	<i>vanLeerV</i>	Similar to VanLeer scheme ⁵⁷ modified for vector field
$\nabla \cdot (\vec{U} \alpha_L), \nabla \cdot (\rho \vec{U}T)$	<i>vanLeer</i>	See Ref. 57
$\nabla \cdot (\vec{U}_c \alpha_L (1 - \alpha_L))$	<i>InterfaceCompression</i>	See Ref. 58
$\nabla \chi^*$	<i>Linear</i>	Central difference schemes
$\nabla \frac{1}{f} \chi^{**}$	<i>corrected</i>	Surface normal gradient with correction on non-orthogonal meshes ⁵⁹
$\nabla \cdot (\chi_1 \nabla \chi_2)$	<i>Linear corrected</i>	Face values (χ_1) approximated by central difference scheme, and the resulting surface normal gradient is calculated using central difference schemes with non-orthogonal correction
Term	Interpolation scheme	Method
χ_f	<i>Linear</i>	Default interpolation schemes for getting face values from cell values

χ : volScalarField or volVectorField

χ_f : surfaceScalarField or surfaceVectorField

equilibrium. Evaporation pushes liquid away from the heated wall. The analytical solution for interface position $\delta(t)$ and temperature $T(x, t)$ on the vapor side are given by¹⁶

$$\delta_{an}(t) = 2\eta\sqrt{d_G t}, \quad (29)$$

$$T(x, t) = T_w + \frac{T_{sat} - T_w}{erf(\eta)} erf\left(\frac{x}{2\sqrt{d_G t}}\right), \quad (30)$$

where d_G is vapor thermal diffusivity, and η is determined from

$$\eta \exp(\eta^2) erf(\eta) = \frac{c_{pG}(T_w - T_{sat})}{\sqrt{\pi} H_{LG}}. \quad (31)$$

A quasi 1D computational domain with only one grid cell in the direction of translational invariance is considered. A very thin vapor film is inserted in the computational domain in the initial time near the hot wall. The liquid-vapor thermo physical properties for water at saturation pressure 1.0 Mpa are chosen which correspond to the moderate density ratio of ($\frac{\rho_L}{\rho_G} \approx 170$). In order to ensure that the coefficient of mass flux rate in the energy equation is constant in the CFD model during the phase change process, liquid and vapor phases specific heat are assumed equal ($C_{pG} = C_{pL}(P_{sat})$). A schematic of Stefan problem is illustrated in Fig. 8. A no slip boundary condition is employed for the velocity boundary condition at the hot wall. Temperature of the super-heated wall is 10K higher than saturation temperature.

The integrated simulation error is estimated as the film thickness error ($|\delta_{sim} - \delta_{an}|$) summed over time steps i , weighted by time step (Δt):

$$E = \sum_i |\delta_{sim} - \delta_{an}| \Delta t. \quad (32)$$

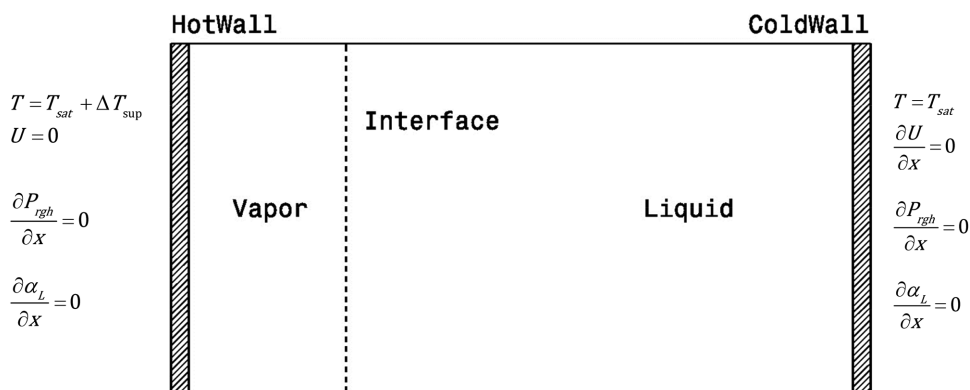


FIGURE 8 Schematic of Stefan problem, boundary conditions, $P_{sat} = 1 \text{ Mpa}$, $T_{sat} = 453.03 \text{ K}$, $\Delta T_{sup} = 10 \text{ K}$

TABLE 3 Stefan problem convergence

	Cell Number	Numerical Simulation			Exact
		128	256	512	
Lee	Final Thickness (mm)	1.88514	1.88228	1.87743	1.86722
	Error (mm.s)	0.83902	0.65766	0.48976	
Tanasawa	Final Thickness (mm)	1.88093	1.88001	1.88084	
	Error (mm.s)	0.51143	0.53373	0.62118	

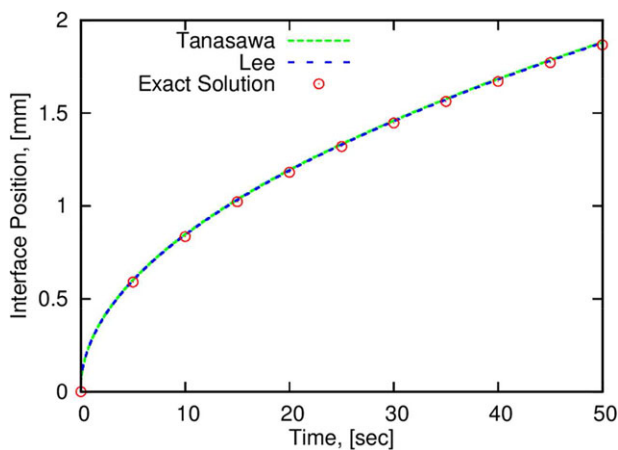


FIGURE 9 Interface position in Stefan problem, compare exact solution with present numerical simulations (Lee and Tanasawa), $P_{sat} = 1 \text{ Mpa}$ and $r_e = 10^5$, $\gamma = 1.0$

Simulation is conducted on three different grids with 128, 256, and 512 cells. The final interface position is at $t = 50 \text{ (s)}$ and the integrated errors are display in Table 3. It shows the numerical error in the Tanasawa model is smaller than the Lee model on coarse grids. Furthermore, the numerical error becomes smaller on finer grids in the Lee model, but remains constant in the Tanasawa model.

The interface position (δ) and dimensionless temperature ($\theta = \frac{T - T_w}{T_{sat} - T_w}$) are displayed in Figs. 9 and 10, respectively. It can be seen there is excellent agreement between CFD results and the exact solution.

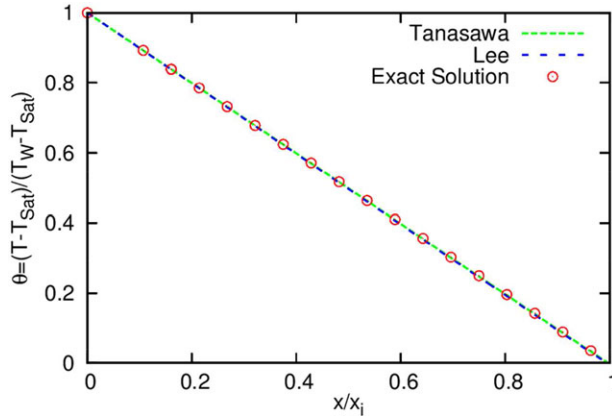


FIGURE 10 Dimensionless temperature in Stefan problem, compare exact solution with present numerical simulations (Lee and Tanasawa), $P_{sat} = 1 \text{ Mpa}$ and $r_e = 10^5$, $\gamma = 1.0$

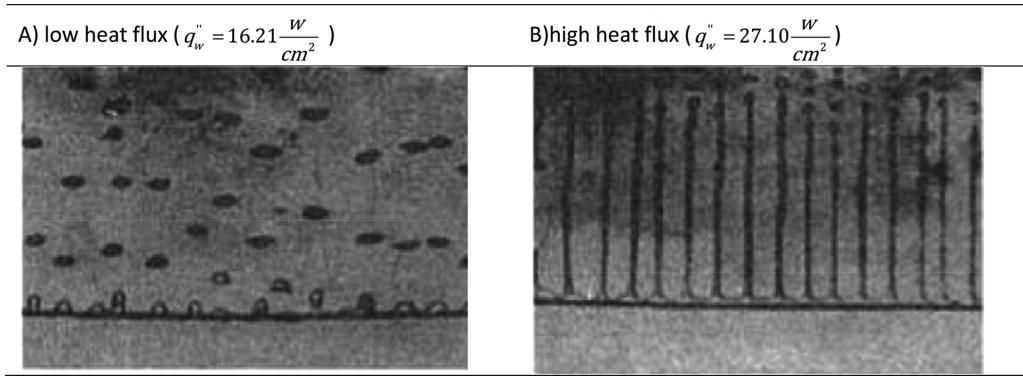


FIGURE 11 Hydrodynamic transition in bubble release pattern observed by Reiman and Grigg⁶³

3.2 | 2D-film boiling

Boiling of quiescent liquid near a hot solid surface is known as pool boiling. Some major regimes in pool boiling are convective heat transfer, nucleation boiling, and film boiling. In film boiling, a vapor layer separates saturated or sub-cooled liquid from the hot solid plate. Due to the liquid's higher density compared to vapor, Rayleigh–Taylor instability occurs which amplifies small perturbations at the interface and leads to bubble growth. Figure 11 indicates that the bubble is released individually and sequentially for the low heat flux situation, and columns are found for the high heat flux one. This problem has no analytical solution. Therefore, numerical simulations are compared with previous numerical work using the sharp interface method and the widely accepted correlations of Berenson⁶² for the Nusselt number

$$Nu_{Be} = 0.425 \left(\frac{\rho_G(\rho_L - \rho_G)gH_{LG}}{k_G\mu_G[T_w - T_{sat}]} \right)^{1/4} \lambda^{3/4}, \quad (33)$$

where λ is the characteristic length and given by

$$\lambda = \sqrt{\frac{\sigma}{(\rho_L - \rho_G)g}}. \quad (34)$$

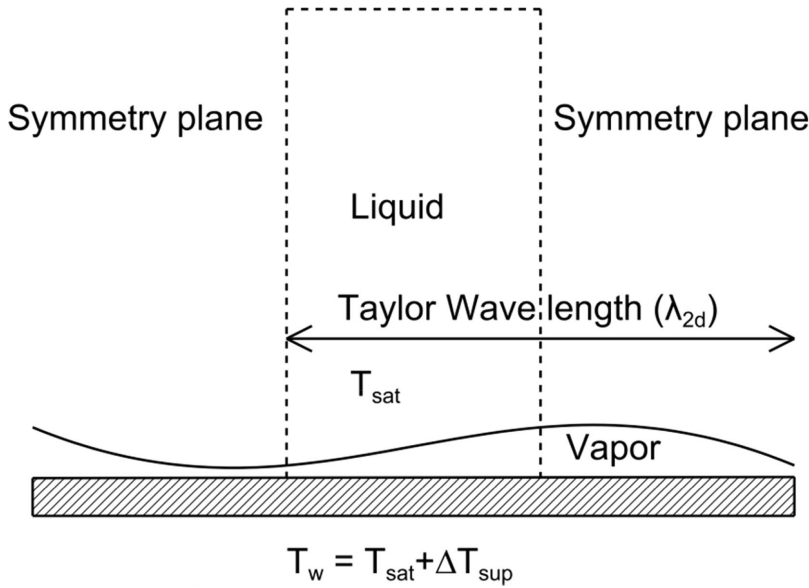


FIGURE 12 Two-dimensional film boiling, dash line is computational domain, $P_{sat} = 21.9 \text{ Mpa}$

For numerical simulation of two-dimensional film boiling, two scenarios have been reported in the literature:

1. Quasi-periodic

Bubble pinch off occurs individually in the node^{16,64} or happens sequentially between node and anti-node^{23,64} and creates a quasi-periodic pattern.

2. Bubble column

The vapor bubble is connected to the vapor film with a thin neck and creates a mushroom shape.^{16,17,22,65} Some researchers have noted that 2D numerical simulations cannot be expected to give an accurate representation of the 3D physics of film boiling. Furthermore, the two-dimensional simulation only considers the components of the interface curvature lying in the computational plane, whereas the out-of-plane components are neglected. In other word, surface tension driving hydrodynamic instabilities usually cannot be captured in a realistic way¹⁷ and Rayleigh–Plateau instability which plays a role in bubble pinch off may never show up in the 2D model.^{17,22}

The sharp interface method was conducted in all previous studies on the numerical simulation of film boiling,^{16,17,22,23,64,66} hence, the present numerical study using the diffuse interface method is compared with them. Here, the film boiling problems are set similar to Tomar²³ and Guo⁶⁴ works which are for saturated water at near critical pressure $P_{sat} = 21.9 \text{ Mpa}$. They simulated film boiling using the couple of level set and VOF method (CLSVOF²³ and VOSET⁶⁴) with a sharp mass transfer model. Additionally, Guo⁶⁴ applied a PLIC method for interface reconstruction to gain more accuracy. A schematic of two-dimensional film boiling is illustrated in Fig. 12. The super-heated wall temperature is set 10k and 30K above the saturation temperature. The wall boundary condition is

$$\text{at } y = 0 : \vec{U} = (0, 0), \quad T = T_{sat} + \Delta T_{sup}, \quad \frac{\partial P_{rgh}}{\partial y} = \frac{\partial \alpha_L}{\partial y} = 0. \quad (35)$$

The outflow boundary condition is

$$\text{at } y = H : P_{rgh} = P_{sat}, \quad \frac{\partial T}{\partial y} = \frac{\partial \alpha_L}{\partial y} = \frac{\partial \vec{U}}{\partial y} = 0. \quad (36)$$

At the beginning of simulation, a vapor film is inserted in the computational domain. Vapor film thickness is given by⁶⁶

$$y = y_c + \varepsilon \cos\left(\frac{\pi N x}{W}\right), \quad (37)$$

where y_c , ε and N are unperturbed film thickness, perturbation amplitude and perturbation wave, respectively. The following values are chosen for the present simulation:

$$y_c = \frac{4.0}{128} \lambda_{2d}, \quad \varepsilon = \frac{1}{128} \lambda_{2d}, \quad N = 1, \quad W = \lambda_{2d}/2, \quad (38)$$

where λ_{2d} is the most unstable Taylor in viscid wavelength for two-dimensional horizontal flat surfaces and is defined as

$$\lambda_{2d} = 2\pi \sqrt{\frac{3\sigma}{g(\rho_L - \rho_G)}}. \quad (39)$$

Nusselt number is computed as the dimensionless heat flux through the wall and is given by

$$Nu_{2d} = \frac{\int_0^W \left(\frac{\lambda}{T_w - T_{sat}} \times \frac{\partial T}{\partial y} \Big|_{y=0} \right) dx}{W}, \quad (40)$$

where W is the computational domain width which is $\lambda_{2d}/2$. The computational domain height is λ_{2d} in the present simulations.

The grid independence test is conducted with different grid sizes using the Tanasawa mass transfer model. Figure 13 depicts the interface as the first bubble is going to leave the vapor film. The bubble detachment time from the thin vapor neck is dependent on grid size, because the interface breaks whenever the thickness of neck falls below the specific resolved grids. Therefore, in the coarse grid (120×240) the bubble leaves the vapor film sooner. There is no significant change in bubble shape between the two last finer grids, so a grid with 240×480 cells is chosen for the film boiling simulations.

Figure 14 shows the quasi-periodic release of bubble from node and anti-node. The temperature of the solid wall is set at 10K above saturation temperature. With the given initial interface, a bubble is formed at the node (center). Then, the bubble leaves the film under the effect of buoyancy. After detachment, the vapor neck returns to the wall due to surface tension and moves to the anti-node lead bubble growth on the outer side. The present numerical result is in good agreement with the numerical results of Refs. 64 and 23 in predicting the bubble release pattern, bubble shape, and first detachment time of bubble. The space-averaged Nusselt number over time is shown in Fig. 15. The Nusselt number depends strongly on the film thickness. Heat flux is greater where the vapor film is thin and less when the film is the thick. Therefore, average heat flux and Nusselt number increase when the vapor rushes to fill the bubble and the remaining film becomes thin. To the contrary, after detachment, the vapor returns to the superheated wall and increased film thickness leads to a smaller Nusselt number. The Nusselt number predicted by Berenson's correlation is 3.69. The computed time and space averaged Nusselt number is 2.57 and 2.64 for the Tanasawa and Lee models, respectively. The difference is about 28% and 30%. Guo et al.⁶⁴ and Tomar et al.²³ obtained average Nusselt numbers of 4.67 and

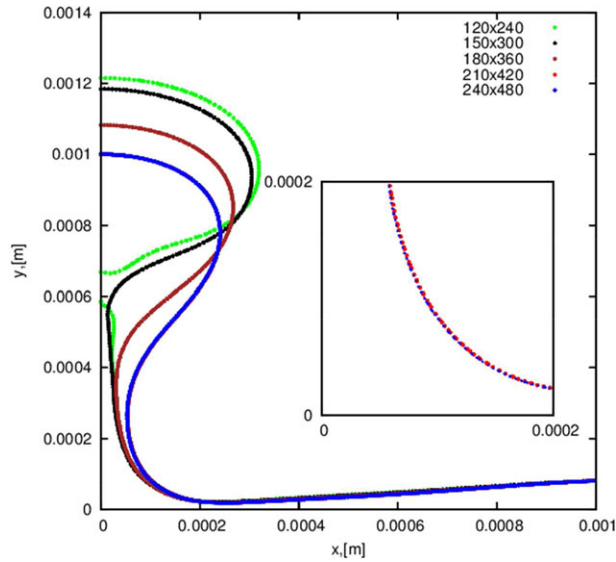


FIGURE 13 Bubble shape at five grids before the first detachment at $t = 0.32$ s, the grids 210×420 and 240×480 have almost the same shape, $P_{sat} = 21.9 \text{ Mpa}$, $\Delta T_{sup} = 10 \text{ K}$

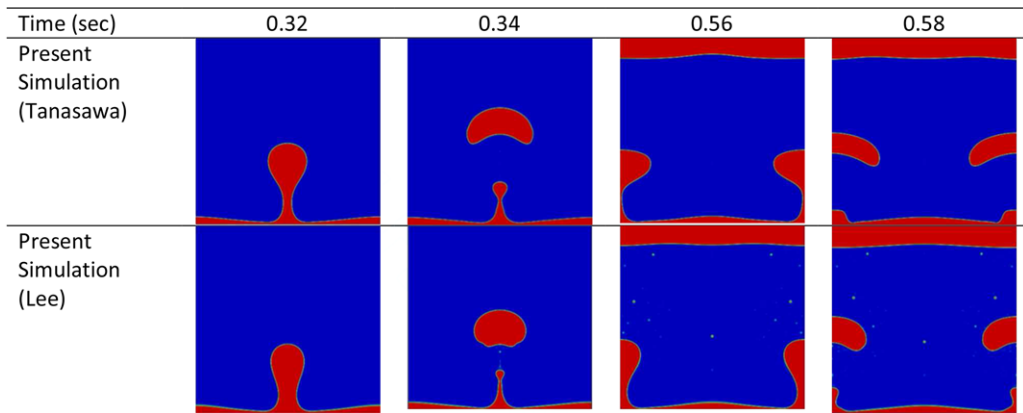


FIGURE 14 Bubble shapes at different instants. $P_{sat} = 21.9 \text{ Mpa}$, $\Delta T_{sup} = 10 \text{ K}$

5.37 for a similar problem, corresponding to 27% and 45% difference, respectively. This shows the present numerical errors are in the range of previous numerical simulations.

The second series of simulation were performed with a wall superheat of 30K above saturation temperature. Figure 16 shows the interface evolution at different time instants. For this case, Lee's mass transfer model still predicts the quasi periodic release of the bubble, but Tanasawa's mass transfer model predicts a tall and stable vapor column which is similar with numerical studies of Refs. 23 and 64. The difference may exist due to how these models calculate transferred mass flux rate during the boiling process. In Lee's model, phase change does not need any initial interface. The evaporation takes place wherever in the liquid phase with the temperature above saturation temperature, thus several small bubbles can also be seen in the CFD result in Fig. 16 using Lee's model. In contrast, Tanasawa's model is similar to the sharp interface model, mass transfer only occurs across the existing interface.

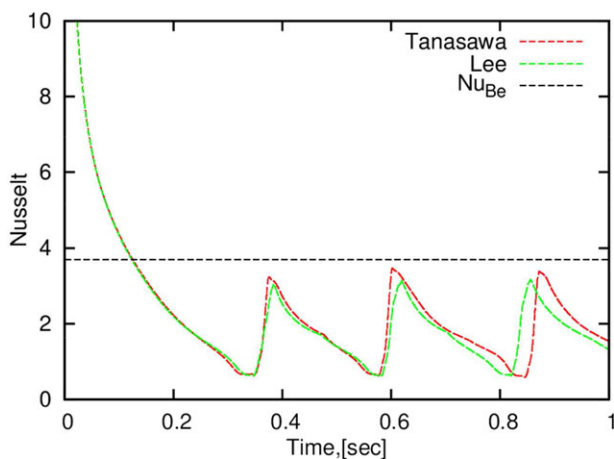


FIGURE 15 Simulation results (Lee and Tanasawa) for space-averaged Nusselt number compare with Berenson correlation, $P_{sat} = 21.9 \text{ Mpa}$, $\Delta T_{sup} = 10 \text{ K}$

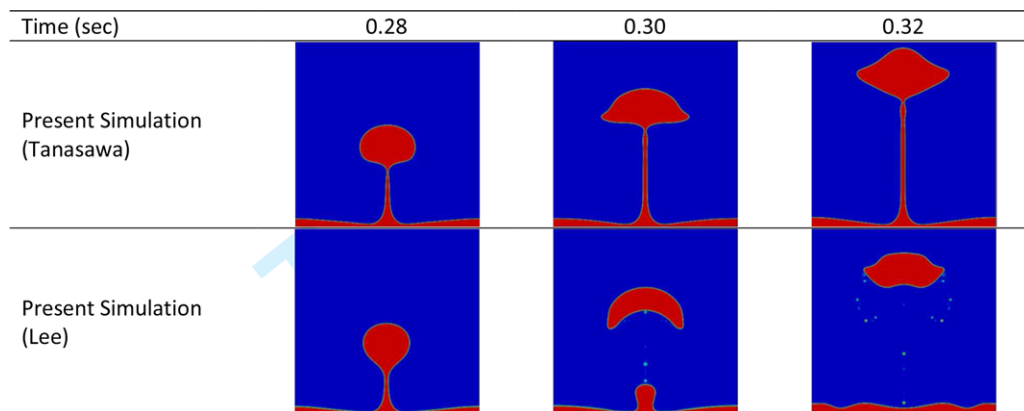


FIGURE 16 Bubble shapes at different instants. $P_{sat} = 21.9 \text{ Mpa}$, $\Delta T_{sup} = 30 \text{ K}$

The space averaged Nusselt number over time for this case is depicted in Fig. 17. It can be found that when vapor film is stable, the space averaged Nusselt number is almost uniform. Lee's model predicts a higher Nusselt number, because after bubble detachment, the vapor rushes back to the wall and increases the heat convection mode near the heated wall. The computed time and space averaged Nusselt number is 2.04 and 2.71 for Tanasawa and Lee models, respectively. The Nusselt number from Berenson's correlation is 2.81, therefore, the difference is 44% and 26%, respectively.

3.3 | Horizontal film condensation

There are two forms of condensation process: dropwise and filmwise condensation.⁶⁷ Dropwise condensation usually occurs when the condensate does not wet the surface and therefore it takes the shape of droplets instead of spreading into a thin film. The filmwise condensation generally prevails on hydrophilic surfaces where a stable thin condensing film will be formed.

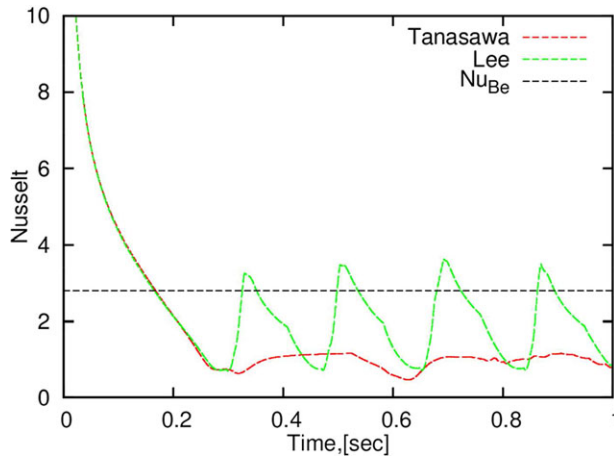


FIGURE 17 Simulation results (Lee and Tanasawa) for space-averaged Nusselt number compare with Berenson correlation, $P_{sat} = 21.9 \text{ Mpa}$, $\Delta T_{sup} = 30 \text{ K}$

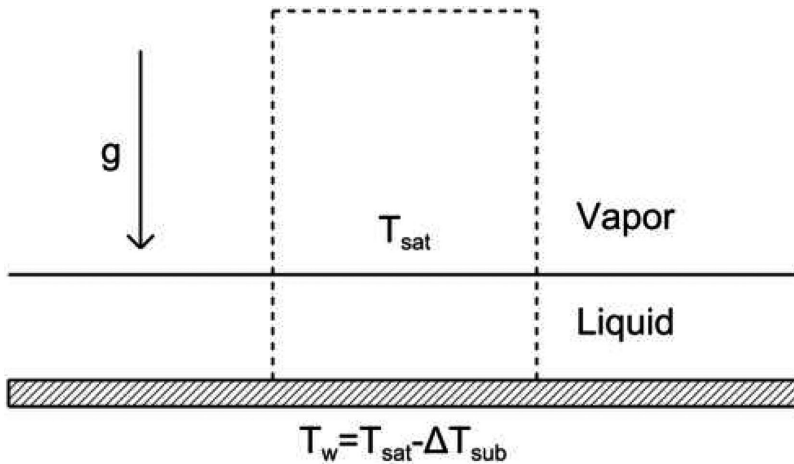


FIGURE 18 Horizontal film condensation, $P_{sat} = 1 \text{ Mpa}$, $\Delta T_{sup} = 30 \text{ K}$

In this case, vapor condenses to form a liquid film on the top surfaces of an isothermal plate at T_w . By assuming a linear temperature profile from T_w at the lower wall to T_{sat} at the interface, a control volume analysis leads to an analytical solution for the film thickness $\delta(t)$:³³

$$\delta_{an}(t) = \left[2t \frac{k_L}{\rho_L C_{pL}} \left(\frac{1}{2} + \frac{H_{LG}}{C_{pL} \Delta T} \right)^{-1} \right]^{1/2}. \quad (41)$$

Relevant thermo physical properties are for saturated water at $P_{sat} = 1 \text{ Mpa}$. Simulation of fluids with greater liquid to vapor property ratios and phase change enthalpies require finer meshes and smaller time steps to adequately resolve the increased range of scales and heat and mass flux magnitudes. Thus, the domain represents a section of an infinitely wide condensing film, a quasi 1D computational domain with only one grid cell in the direction of the translational invariance is considered. The top free stream boundary is set to saturation temperature $T_{sat} = 453.03 \text{ K}$ and the bottom wall is set $T_w = 423.03 \text{ K}$ which corresponds to a 30K subcooled temperature. All fluid entering through

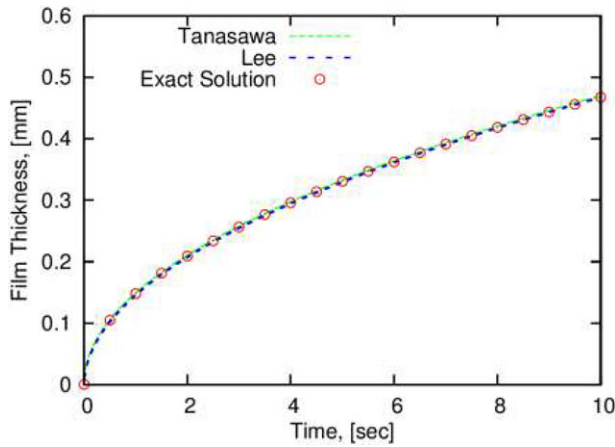


FIGURE 19 Film thickness in horizontal film condensation, compare exact solution with present numerical simulations (Lee and Tanasawa), $P_{sat} = 1 \text{ Mpa}$ and $r_c = 10^5$, $\gamma = 1.0$

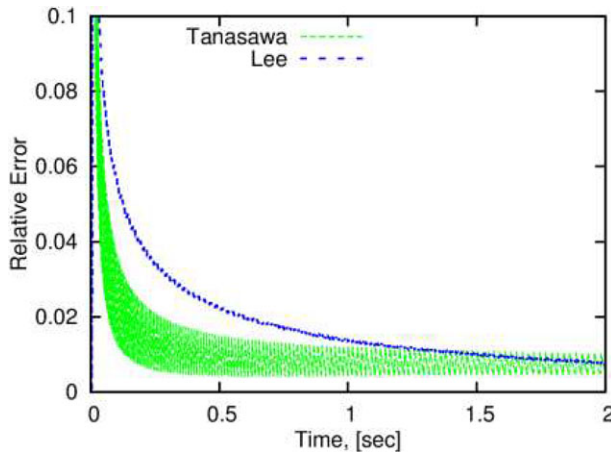


FIGURE 20 Relative error in horizontal film condensation simulations (Lee and Tanasawa), $P_{sat} = 1 \text{ Mpa}$ and $r_c = 10^5$, $\gamma = 1.0$

the free stream boundary is vapor. In the beginning of simulation, a very thin film is inserted in the computational domain.

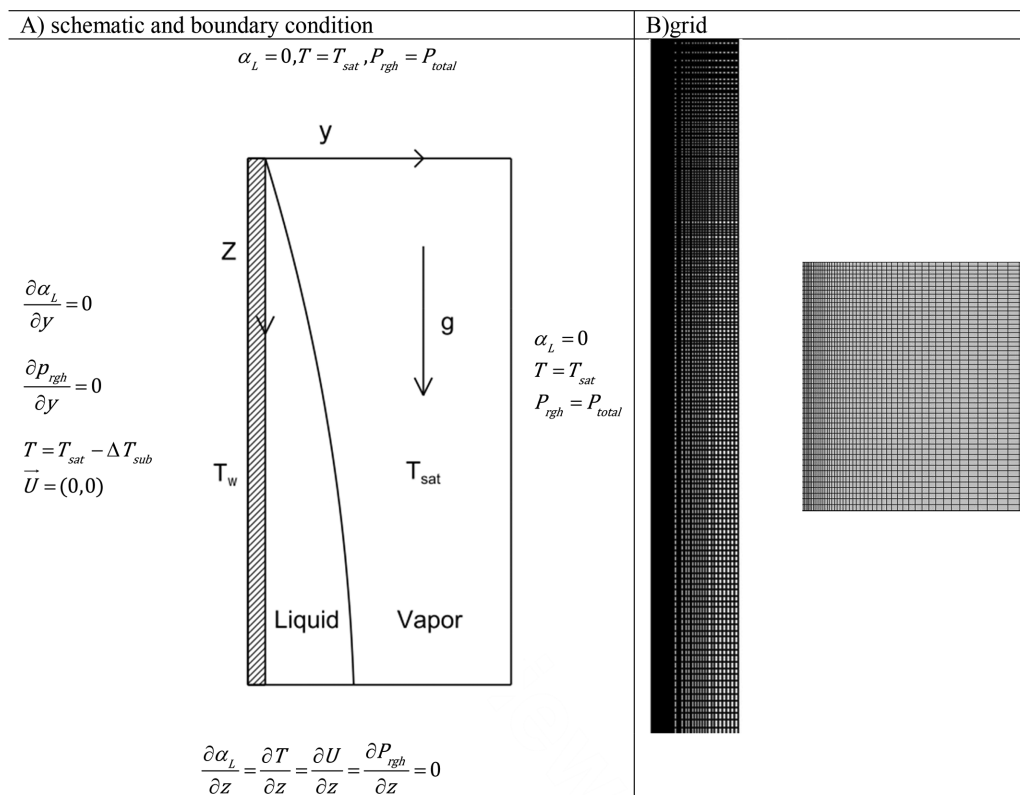
The development of the liquid film thicknesses and relative errors are presented in Figs. 19 and 20, respectively. The simulation relative error is defined as

$$rE = \frac{\delta_{sim} - \delta_{an}}{\delta_{an}}. \quad (42)$$

Relative errors in predicted film thickness are higher during the beginning of simulations, because the liquid films are initially under resolved on fixed meshes. Relative error is smoother and higher in Lee's model than Tanasawa's model. Integrated simulation error was defined in Eq. (32) and presented in Table 4. These results indicate an excellent agreement between both mass transfer models with the analytical solution.

TABLE 4 Convergence study on horizontal film condensation

	Cell Number	Numerical Simulation			Exact
		128	256	512	
Lee	film Thickness (mm)	0.46845	0.467253	0.467361	0.467829
	Error ($\mu\text{m.s}$)	11.3	8.82	9.09	
Tanasawa	film Thickness (mm)	0.469314	0.471797	0.47051	
	Error ($\mu\text{m.s}$)	28.1	24.4	21.6	

**FIGURE 21** Laminar film condensation on a vertical plate, boundary conditions and grid

3.4 | Laminar film condensation on a vertical plate

A sketch of the physical problem of laminar film condensation on a vertical plate is shown in Fig. 21. Where z -axis is along the plate and the y -axis is perpendicular to the plate. The hydrophilic flat plate maintained at a uniform subcooled temperature T_w is suspended in a large volume of vapor at a saturation temperature T_{sat} . Nusselt⁶⁸ studied the steady laminar film condensation by (i) assuming the vapor and liquid film are divided by a sharp interface, (ii) assuming a linear temperature profile across the condensate, (iii) neglecting effects of inertia forces and interface shearing stress. The obtained analytical expression for the film thickness (δ_F) is:

$$\delta_F = \left[\frac{4\mu_L k_L (T_{sat} - T_w) z}{g H_{LG} \rho_L (\rho_L - \rho_G)} \right]^{1/4}. \quad (43)$$

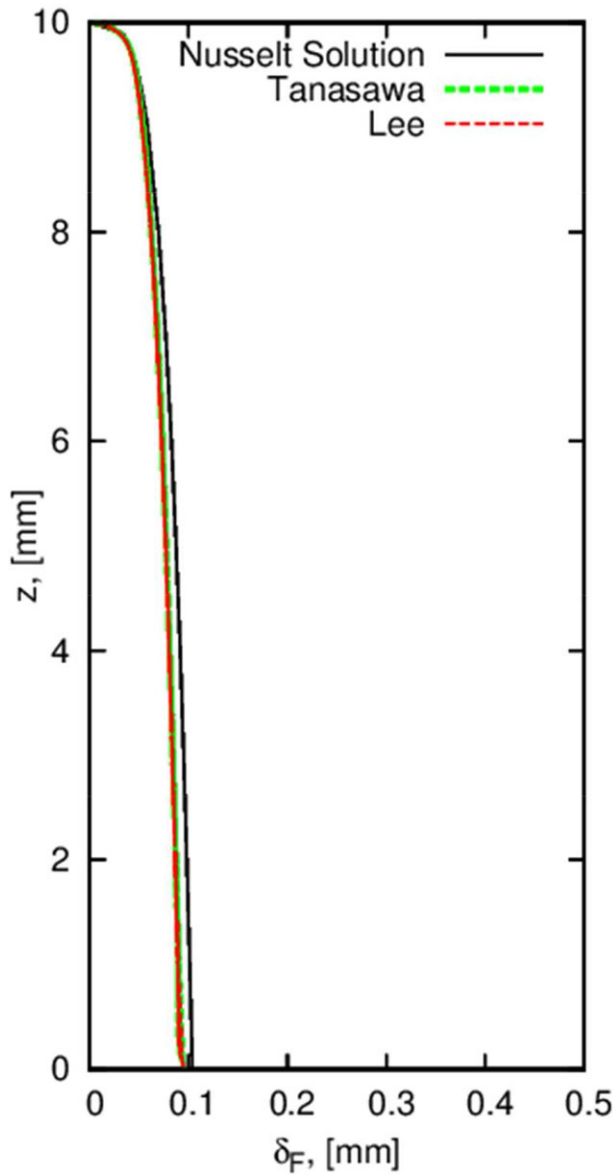


FIGURE 22 Comparison of film thickness given by present numerical simulations (Tanasawa and Lee) and Nusselt's solution

And the velocity distribution in the condensate is given by:

$$U(y) = \frac{g(\rho_L - \rho_G)}{\mu_L} \left(\delta y - \frac{1}{2} y^2 \right). \quad (44)$$

It is assumed in Nusselt's solution that the vapor velocity is zero.

In this section, laminar film condensation on the vertical plate is simulated and numerical results are compared with Nusselt's solution. The material property is for saturated water at $P_{sat} = 21.9 \text{ Mpa}$. A 2D rectangular domain is employed with horizontal and vertical dimensions of 0.5 mm and 10 mm. The mesh is defined with 100×300 cells which is grading in the horizontal and vertical direction with

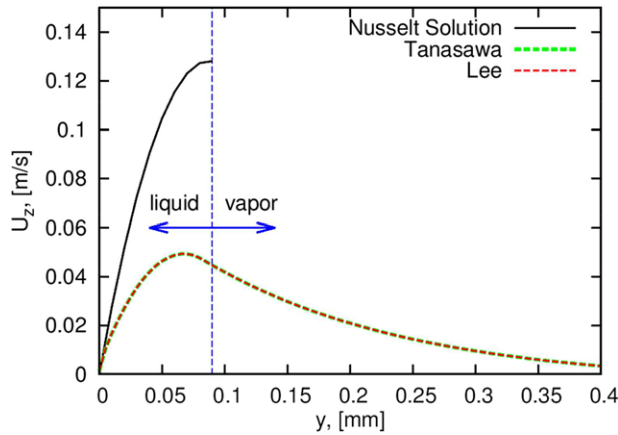


FIGURE 23 Comparison velocity distribution at $z = 5$ mm given by present numerical simulations (Lee and Tanasawa) and Nusselt's solution

cells in a row near the wall or inlet is 0.1 the height of the cells row near free stream or outlet, respectively. The wall is 20 K subcooled. The boundary conditions and mesh is illustrated at Fig. 21. For the vapor side, total pressure is assigned for pressure and velocity is calculated from the pressure boundary condition.

Simulation is conducted for 2 seconds to reach steady state condition. Assuming negligible interfacial shear, the wall shear stress can be evaluated as $\tau_w = \rho_L g \delta$ and dimensionless wall distance as $y^+ = \frac{\sqrt{g \delta} y}{\nu_L}$ where y is the cell center distance to the nearest wall and ν_L is the liquid kinematic viscosity. In the present simulation y^+ is smaller than 3. This low value of y^+ indicates that near wall fluid and heat transfer physics are well resolved. Figure 22 shows the liquid film thickness at steady state determined from numerical result using Tanasawa's and Lee's models. It is seen that the liquid film thickness obtained from the present numerical simulation agrees well with the classical Nusselt analytical prediction.

The velocity profile from the numerical simulation is compared with Nusselt's solution in Fig. 23. The velocity increases from zero at the wall to a maximum value away from the wall and then decreases monotonically to zero in the vapor at infinity. Thus, the velocity profile is continuous from the subcooled liquid at the wall to dry vapor at infinity. The velocity profile given by the Nusselt model is discontinuous. It can be seen that the velocity obtained by both mass transfer models are the same and they are smaller than that of the classical Nusselt model given by Eq. (44). Because the classical Nusselt model did not take into consideration the effects of inertia forces, convection terms and interfaces shear stress. In contrast, these three parameters are taken into consideration in the numerical simulations. Therefore, the film liquid induces the vapor flow and at the same time, liquid film gives up some of its momentum, and therefore its velocity decreases as compared to that given by Eq. (44). A similar result for the velocity profile is pointed out in numerical results of Liu and Cheng⁶⁹ who simulated laminar film condensation with the Lattice Boltzman method.

The dimensionless temperature defined as $\theta = \frac{T - T_w}{T_{sat} - T_w}$ is presented in Fig. 24. Nusselt's solution assumed a linear variation of temperature within the liquid film and constant saturation temperature outside of the condensate liquid film. Numerical simulation shows for the present thermophysical properties and film thickness the linear variation of temperature in the liquid film is not valid.

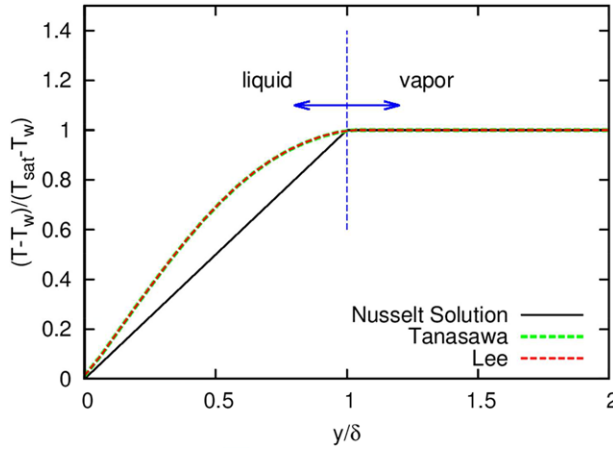


FIGURE 24 Temperature profiles at $z = 5$ mm in film condensation on a vertical flat plate, compare present numerical simulations (Tanasawa and Lee) and Nusselt's solution

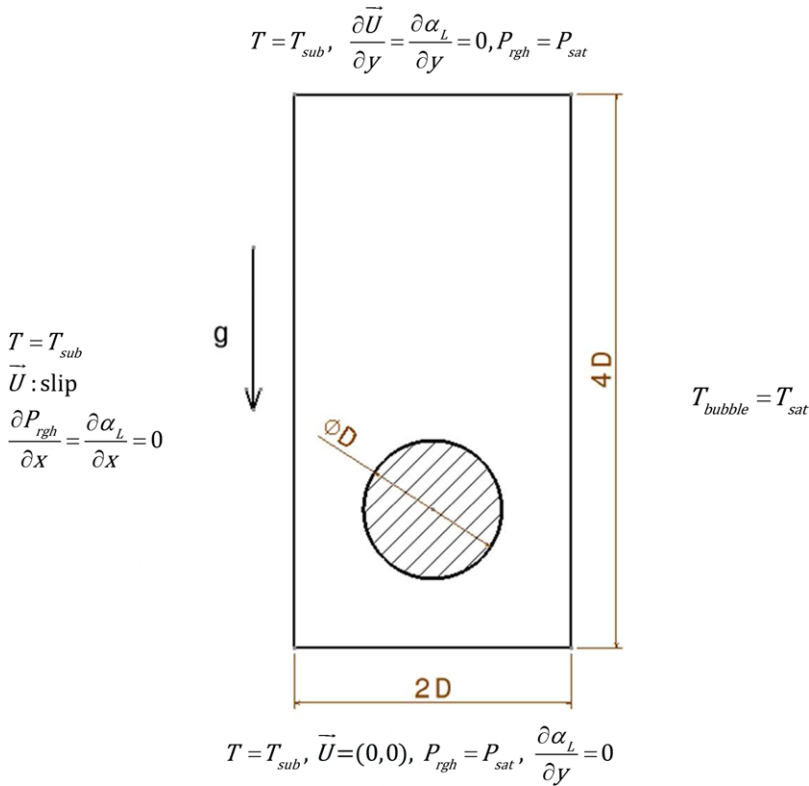


FIGURE 25 Schematic of bubble condensation in subcooled boiling, initial and boundary conditions

3.5 | Bubble condensation

Bubble condensation is one of the fundamental issues in a subcooled flow boiling to describe the heat and mass transfer. In this section, the rising of a single vapor bubble in quiescent subcooled water is simulated. The geometry of the considered problem and applied boundary condition are illustrated

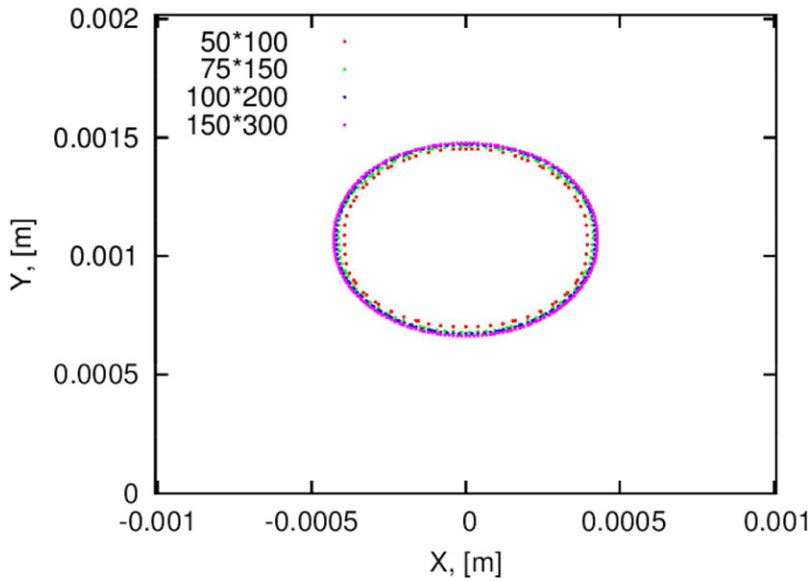


FIGURE 26 Bubble shape at $t = 1\text{ms}$ for different grids, $P_{sat} = 0.130\text{[Mpa]}$ and $\Delta T_{sub} = 25\text{[K]}$

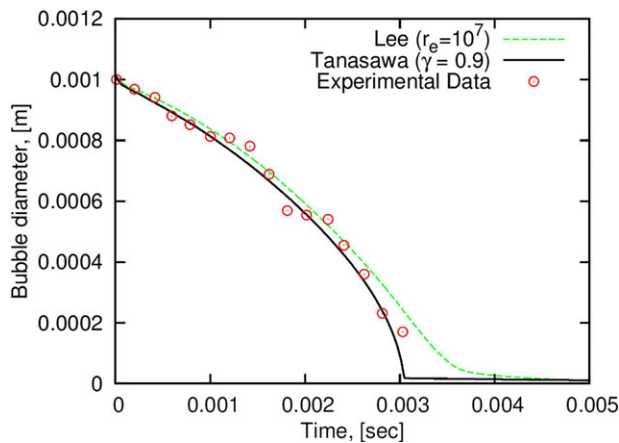


FIGURE 27 Bubble diameter history, compare between present numerical simulations and experimental data,⁷⁰ $D_0 = 1.008\text{mm}$, $P_{sat} = 0.130\text{[Mpa]}$ and $\Delta T_{sub} = 25\text{[K]}$

in Fig. 25 which is similar to Samkhaniani and Ansari.⁷¹ The 2D space domain is set as $2D_0 \times 4D_0$ where D_0 is the initial diameter of vapor bubble. The bubble is located in the position of (D_0, D_0) at the beginning of the simulation.

A mesh resolution analysis is performed on four different grids using Tanasawa's model to figure out the appropriate grid size for simulation of bubble condensation. These grids are 50×100 , 75×150 , 100×200 , and 150×300 which, respectively, represent 25, 37, 50, and 75 cells across the initial diameter. It can be seen obviously in Fig. 26 that bubble shape becomes stable with meshes of 100×200 and 150×300 . The variation between the two lateral grids is negligible. Therefore, the bubble is resolved using 100×200 cells in this study.

In order to validate the present numerical simulation, the shape and the bubble diameter history is compared with published experimental results⁷⁰ under saturation pressure 0.130 Mpa for water

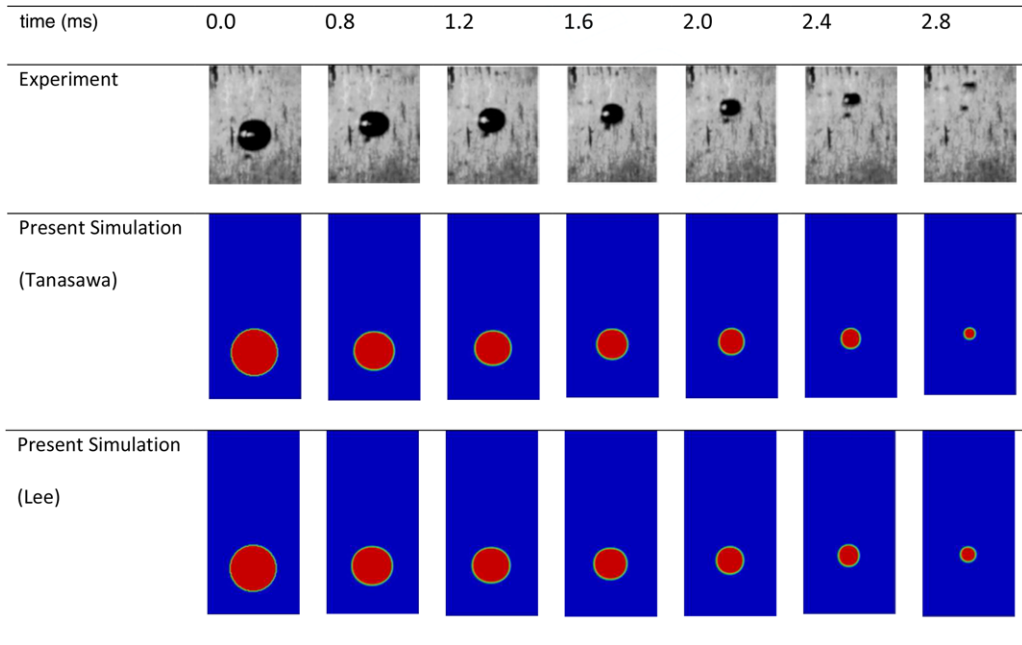


FIGURE 28 Bubble shape, comparison between present numerical results (Lee and Tanasawa) and experimental data,⁷⁰ $D_0 = 1.008\text{mm}$, $P_{sat} = 0.130[\text{Mpa}]$ and $\Delta T_{sub} = 25[\text{K}]$

corresponding to the severe density ratio of ($\frac{\rho_L}{\rho_G} \approx 1263$). The comparison of bubble diameter history is shown in Fig. 27 and the bubble shape in Fig. 28. Bubble diameter in 2D simulation is the diameter of an equivalent circle. It can be seen that numerical result is in reasonable good agreement with the experimental results.

4. | CONCLUSION

In the present study, a new solver called *phaseChangeHeatFoam* is implemented in the OpenFOAM cfd package to simulate boiling and condensation processes. For now, two mass transfer models (Lee and Tanasawa) are implemented in the solver. However, adding a new mass transfer model is straight forward. The governing equations and programming information are discussed in detail. This solver is based on the CF-VOF method, but spurious current is reduced by using a filter method for calculation of the interface curvature. The present numerical simulations are compared with analytical solutions, previous sharp interface method results and experimental data for different thermo-physical properties. Our investigation shows the present diffuse interface method is capable of accurate simulation of the phase change process even for a severe ratio of thermophysical properties ($\frac{\rho_L}{\rho_v} \approx 1000$). Additionally, the performance of Lee and Tanasawa mass transfer models are investigated here through simulations, it was found both mass transfer models have similar performance in simple simulations (Stefan and horizontal film condensation). However, in the simulation of complex phenomena, for instance film boiling, the difference in the numerical results obtained with Lee and Tanasawa mass transfer models can be considerable. Our study shows numerical results with Tanasawa mass transfer model are very similar to the sharp interface model.

APPENDIX A: THERMOPHYSICAL PROPERTIES OF SATURATED WATER

Liquid							
$T[K]$	$P[MPa]$	$\rho[\frac{kg}{m^3}]$	$H[\frac{kJ}{kg}]$	$C_p[\frac{kJ}{kg.K}]$	$\mu[Pa.s]$	$k[\frac{W}{m.K}]$	$\sigma[\frac{N}{m}]$
380.26	0.13	953.13	449.19	4.2244	2.620E-04	0.68106	0.05753
453.03	1	887.13	762.52	4.4045	1.5024E-4	0.67337	0.042217
646	21.9	402.4	1963.5	218	4.67E-05	0.545	0.00007
Vapor							
$T[K]$	$P[MPa]$	$\rho[\frac{kg}{m^3}]$	$H[\frac{kJ}{kg}]$	$C_p[\frac{kJ}{kg.K}]$	$\mu[Pa.s]$	$k[\frac{W}{m.K}]$	
380.26	0.13	0.7545	2686.6	2.1107	1.251E-05	0.02590	
453.03	1	5.1450	2777.1	2.7114	1.502E-05	0.03643	
646	21.9	242.7	2240	352	3.23E-06	0.538	

REFERENCES

- Gingold RA, Monaghan JJ. Smoothed particle hydrodynamics: theory and application to non-spherical stars. *Mon Not R Astron Soc.* 1977;181:375–389.
- Unverdi SO, Tryggvason G. A front-tracking method for viscous, incompressible, multi-fluid flows. *J Comput Phys.* 1992;100:25–37.
- Sussman M, Smereka P, Osher S. A level set approach for computing solutions to incompressible two-phase flow. *J Comput Phys.* 1995;114:146–159.
- Hirt CW, Nichols BD. Volume of fluid (VOF) method for the dynamics of free boundaries. *J Comput Phys.* 1981;39:201–225.
- Worner M. Numerical modeling of multiphase flow in microfluidics and micro process engineering: a review of methods and applications. *Microfluid NanoFluid.* 2012;12:841–886.
- Sussman M, Puckett EG. A coupled level set and volume-of-fluid method for computing 3D and axisymmetric incompressible two-phase flows. *J Comput Phys.* 2000;162:301–337.
- Sussman M. A second order coupled level set and volume-of-fluid method for computing growth and collapse of vapor bubbles. *J Comput Phys.* 2003;187:110–136.
- Van der Pijl S, Segal A, Vuik C, Wesseling P. A mass conserving level set method for modelling of multi-phase flows. *Int J Numer Methods Fluids.* 2005;47:339–361.
- Lv X, Zou Q, Zhao Y, Reeve D. A novel coupled level set and volume of fluid method for sharp interface capturing on 3D tetrahedral grids. *J Comput Phys.* 2010;229:2573–2604.
- Sun D, Tao W. A coupled volume-of-fluid and level set (VOSET) method for computing incompressible two-phase flows. *Int J Heat Mass Transfer.* 2010;53:645–655.
- Youngs DL. Time-dependent multi-material flow with large fluid distortion. *Num Methods Fluid Dyn.* 1982;24:273–285.
- Renardy Y, Renardy M. PROST: a parabolic reconstruction of surface tension for the volume-of-fluid method. *J Comput Phys.* 2002;183:400–421.
- Ubbink O, Issa R. A method for capturing sharp fluid interfaces on arbitrary meshes. *J Comput Phys.* 1999;153:26–50.
- Xiao F, Honma Y, Kono T. A simple algebraic interface capturing scheme using hyperbolic tangent function. *Int J Numer Methods Fluids.* 2005;48:1023–1040.
- Lyklema J. Fundamentals of Interfaces and Colloid Science, Vol. I: Fundamentals. Academic Press; 1991.
- Welch SWJ, Wilson J. A volume of fluid based method for fluid flows with phase change. *J Comput Phys.* 2000;160:662–682.

17. Hardt S, Wondra F. Evaporation model for interfacial flows based on a continuum-field representation of the source terms. *J Comput Phys*. 2008;227:5871–5895.
18. Schlottke J, Weigand B. Direct numerical simulation of evaporating droplets. *J Comput Phys*. 2008;227:5215–5237.
19. Son G, Dhir V. Numerical simulation of film boiling near critical pressures with a level set method. *J Heat Transfer*. 1998;120:183–192.
20. Son G, Dhir V, Ramanujapu N. Dynamics and heat transfer associated with a single bubble during nucleate boiling on a horizontal surface. *J Heat Transfer*. 1999;121:623–631.
21. Tanguy S, Ménard T, Berlemont A. A level set method for vaporizing two-phase flows. *J Comput Phys*. 2007;221:837–853.
22. Gibou FDR, Chen L, Nguyen D, Banerjee S. A level set based sharp interface method for the multiphase incompressible Navier–Stokes equations with phase change. *Comput Phys*. 2007;222:536–555.
23. Tomar G, Biswas G, Sharma A, Agrawal A. Numerical simulation of bubble growth in film boiling using a coupled level-set and volume-of-fluid method. *Phys Fluids*. 2005;17.
24. Kunkelmann C, Stephan P. Numerical simulation of the transient heat transfer during nucleate boiling of refrigerant HFE-7100. *Int J Refrig*. 2010;33:1221–1228.
25. Weller HG, Taboral G, Jasak H, Fureby C. A tensorial approach to computational continuum mechanics using object-oriented techniques. *Comput Phys*. 1998;12:620–632.
26. Deshpande SS, Anumolu L, Trujillo MF. Evaluating the performance of the two-phase flow solver interFoam. *Comput Sci Discovery*. 2012;5:014016.
27. Berberović E, Hinsberg NPv, Jakirlić S, Roisman IV, Tropea C. Drop impact onto a liquid layer of finite thickness: dynamics of the cavity evolution. *Am Phys Soc*. 2009;79:036306 (15).
28. Klostermann J, Schaake K, Schwarze R. Numerical simulation of a single rising bubble by VOF with surface compression. *Int J Numer Methods Fluids*. 2013;71:960–982.
29. Ubbink O. *Numerical Prediction of Two Fluid Systems with Sharp Interfaces*. London: University of London; 1997.
30. Kunkelmann C, Stephan P. CFD simulation of boiling flows using the volume-of-fluid method within OpenFOAM. *Num Heat Transfer* 2009;56:631–646.
31. Zeng Q, Cai J, Yin H, Yang X, Watanabe T. Numerical simulation of single bubble condensation in subcooled flow using OpenFOAM. *Progress Nucl Energy*. 2015;83:336–346.
32. Doro EO. Computational modeling of falling liquid film free surface evaporation. 2012.
33. Rattner AS, Garimella S. Simple mechanistically consistent formulation for volume-of-fluid based computations of condensing flows. *J Heat Transfer*. 2014;136:071501.
34. Bahreini M, Ramiar A, Ranjbar AA. Numerical simulation of bubble behavior in subcooled flow boiling under velocity and temperature gradient. *Nucl Eng Des*. 2015;293:238–248.
35. Schrage RW. *A Theoretical Study of Interphase Mass Transfer*. Columbia University Press; 1953.
36. Knudsen M. *The Kinetic Theory of Gases: Some Modern Aspects*. Metheun & Company; 1950.
37. Marek R, Straub J. Analysis of the evaporation coefficient and the condensation coefficient of water. *Int J Heat Mass Transfer*. 2001;44:39–53.
38. Tanasawa I. Advances in condensation heat transfer. *Adv Heat Transfer*. 1991;21:55–139.
39. Lee WH. A pressure iteration scheme for two-phase flow modeling. *Multiph Transp Fundam React Saf Appl*. 1980;1:407–431.
40. Sun D-L, Xu J-L, Wang L. Development of a vapor–liquid phase change model for volume-of-fluid method in FLUENT. *Int. Commun Heat Mass Transfer*. 2012;39:1101–1106.
41. Wu H, Peng X, Ye P, Gong YE. Simulation of refrigerant flow boiling in serpentine tubes. *Int J Heat Mass Transfer*. 2007;50:1186–1195.
42. De Schepper SC, Heynderickx GJ, Marin GB. Modeling the evaporation of a hydrocarbon feedstock in the convection section of a steam cracker. *Comput Chem Eng*. 2009;33:122–132.

43. Alizadehdakheel A, Rahimi M, Alsairafi AA. CFD modeling of flow and heat transfer in a thermosyphon. *Int Commun Heat Mass Transfer*. 2010;37:312–318.
44. Yang Z, Peng X, Ye P. Numerical and experimental investigation of two phase flow during boiling in a coiled tube. *Int J Heat Mass Transfer*. 2008;51:1003–1016.
45. Goodson K, Rogacs A, David M, Fang C. Volume of fluid simulation of boiling two-phase flow in a vapor-venting microchannel. *Frontiers Heat Mass Transfer*. 2010;1.
46. Lee H, Kharangate CR, Mascarenhas N, Park I, Mudawar I. Experimental and computational investigation of vertical downflow condensation. *Int J Heat Mass Transfer*. 2015;85:865–879.
47. Albadawi A, Donoghue D, Robinson A, Murray D, Delauré Y. Influence of surface tension implementation in volume of fluid and coupled volume of fluid with level set methods for bubble growth and detachment. *Int J Multiph Flow*. 2013;53:11–28.
48. Samkhaniani N, Gharehbaghi A, Ahmadi Z. Numerical simulation of reaction injection molding with polyurethane foam. *J Cell Plast*. 2013;49:405–421.
49. Marschall H, Hinterberger K, Schuler C, Habla F, Hinrichsen O. Numerical simulation of species transfer across fluid interfaces in free-surface flows using OpenFOAM. *Chem Eng Sci*. 2012;78:111–127.
50. Brackbill JU, Kothe DB, Zemach C. A continuum method for modeling surface tension. *J Comput Phys*. 1992;100:335–354.
51. Scardovelli R, Zaleski S. Direct numerical simulation of free-surface and interfacial flow. *Ann Rev Fluid Mech*. 1999;31:567–603.
52. Lafaurie B, Nardone C, Scardovelli R, Zaleski S, Zanetti G. Modelling merging and fragmentation in multiphase flows with SURFER. *J Comput Phys*. 1994;113:134–147.
53. Hoang DA, van Steijn V, Portela LM, Kreutzer MT, Kleijn CR. Benchmark numerical simulations of segmented two-phase flows in microchannels using the volume of fluid method. *Comput Fluids*. 2013;86:28–36.
54. Zalesak ST. Fully multidimensional flux-corrected transport algorithms for fluids. *J Comput Phys*. 1979;31:335–362.
55. Issa RI. Solution of the implicitly discretised fluid flow equations by operator-splitting. *J Comput Phys*. 1986;62:40–65.
56. Rhie C, Chow W. Numerical study of the turbulent flow past an airfoil with trailing edge separation. *AIAA J*. 1983;21:1525–1532.
57. Van Leer B. Towards the ultimate conservative difference scheme. II. Monotonicity and conservation combined in a second-order scheme. *J Comput Phys*. 1974;14:361–370.
58. Weller H. A new approach to VOF-based interface capturing methods for incompressible and compressible flow. OpenCFD Ltd, Report TR/HGW/04. 2008.
59. Jasak H. *Error Analysis and Estimation for the Finite Volume Method with Applications to Fluid Flows*: University of London; 1996.
60. Sun D-L, Xu J-L, Wang L. Development of a vapor–liquid phase change model for volume-of-fluid method in FLUENT. *International Communications in Heat and Mass Transfer* 2012;39:1101–1106.
61. Tsujimoto K, Kambayashi Y, Shakouchi T, Ando T. Numerical simulation of gas-liquid two-phase flow with phase change using Cahn-Hilliard equation. *Turbulence Heat Mass Transfer* 2009;6.
62. Berenson P. Film-boiling heat transfer from a horizontal surface. *J Heat Transfer*. 1961;83:351–356.
63. Reimann M, Grigull U. Wärmeübergang bei freier konvektion und flimsieden im kritischen gebiet von wasser und kohlendioxid. *Warmeund Stof-fubertragung*. 1975;8:229–239.
64. Guo DZ, Sun DL, Li ZY, Tao WQ. Phase change heat transfer simulation for boiling bubbles arising from a vapor film by the VOSET method. *Num Heat Transfer*. 2011;59:857–881.
65. Juric D, Tryggvason Gt. Computations of boiling flows. *Int J Multiphase Flow*. 1998;24:387–410.
66. Esmaeeli A, Tryggvason G. Computations of film boiling. Part I: numerical method. *Int J Heat Mass Transfer*. 2004;47.

67. Ghiaasiaan SM. *Two-Phase Flow, Boiling and Condensation in Conventional and Miniature System*. Cambridge University Press; 2008.
68. Nusselt W. The surface condensation of water vapour. *VDI Z*. 1916;60:541–546.
69. Liu X, Cheng P. Lattice Boltzmann simulation of steady laminar film condensation on a vertical hydrophilic sub-cooled flat plate. *Int J Heat Mass Transfer*. 2013;62:507–514.
70. Kamei S, Hirata M. Condensing phenomena of a single vapor bubble into subcooled water. *Exp Heat Transfer*. 1990;3:173–182.
71. Samkhaniani N, Ansari M. Numerical simulation of bubble condensation using CF-VOF. *Progress in Nuclear Energy*. 2016;89:120–131.

How to cite this article: Samkhaniani N, Ansari MR. The evaluation of the diffuse interface method for phase change simulations using OpenFOAM. *Heat Transfer–Asian Research*. 2017;46:1173–1203. doi:[10.1002/htj.21268](https://doi.org/10.1002/htj.21268)